Instability-driven electromagnetic fields in coronal plasmas

M. J.-E. Manuel, C. K. Li, F. H. Séguin, N. Sinenian, J. A. Frenje et al.

Citation: Phys. Plasmas **20**, 056301 (2013); doi: 10.1063/1.4801515
View online: http://dx.doi.org/10.1063/1.4801515
View Table of Contents: http://pop.aip.org/resource/1/PHPAEN/v20/i5
Published by the American Institute of Physics.

Instability-driven electromagnetic fields in coronal plasmas[a)]

M. J.-E. Manuel,[1,b),c)] C. K. Li,[1] F. H. Séguin,[1] N. Sinenian,[1] J. A. Frenje,[1] D. T. Casey,[1] R. D. Petrasso,[1] J. D. Hager,[2,d)] R. Betti,[2,e)] S. X. Hu,[2] J. Delettrez,[2] and D. D. Meyerhofer[2,e)]
[1]*Plasma Science and Fusion Center, Massachusetts Institute of Technology, Cambridge, Massachusetts 02139, USA*
[2]*Laboratory for Laser Energetics, University of Rochester, Rochester, New York, 14623, USA*

(Received 16 November 2012; accepted 15 January 2013; published online 15 April 2013)

Filamentary electromagnetic fields previously observed in the coronae of laser-driven spherical targets [F. H. Séguin *et al.*, Phys. Plasma. 19, 012701 (2012)] have been further investigated in laser-irradiated plastic foils. Face-on proton-radiography provides an axial view of these filaments and shows coherent cellular structure regardless of initial foil-surface conditions. The observed cellular fields are shown to have an approximately constant scale size of $\sim$210 μm throughout the plasma evolution. A discussion of possible field-generation mechanisms is provided and it is demonstrated that the likely source of the cellular field structure is the magnetothermal instability. Using predicted temperature and density profiles, the fastest growing modes of this instability were found to be slowly varying in time and consistent with the observed cellular size. © *2013 AIP Publishing LLC*. [http://dx.doi.org/10.1063/1.4801515]

I. INTRODUCTION

Spontaneous electromagnetic fields can be important to the dynamic evolution of a plasma by directing heat flow[1] as well as providing additional pressures on the conducting fluids through the Lorentz force. Electromagnetic fields are predicted to affect fluid behavior during the core-collapse of supernovae[2] through generation of fields due to hydrodynamic instabilities. In the coronae of stars, self-generated magnetic fields lead to filamentary structure[3] in the hot plasma. Recent experiments by Gregori *et al.*[4] investigated sources of protogalactic magnetic fields generated by laser-produced shock waves. In inertial confinement fusion (ICF)[5] experiments, self-generated electromagnetic fields can also play a role. Present day laser facilities provide a unique opportunity to study spontaneous field-generation in these extreme environments under controlled conditions.

Self-generated magnetic fields in laser-produced plasmas were first measured by Stamper *et al.*[6] and were shown to originate from the so-called Biermann battery[7] source caused by misaligned temperature and density gradients. The magnetic field evolution equation is found by substituting the electron momentum equation into Faraday's law and can be expressed as

$$\frac{\partial \mathbf{B}}{\partial t} \approx \frac{\nabla T_e \times \nabla n_e}{e n_e} + \nabla \times (\mathbf{V}_{\text{adv}} \times \mathbf{B}) - \nabla \times (\mathrm{D_m} \nabla \times \mathbf{B}), \quad (1)$$

where T_e is the electron temperature, n_e is the electron density, e is the unit charge, and $\mathrm{D_m}$ is the diffusion coefficient. In this formalism, electron inertia and second order terms in $\mathbf{B}$ have been neglected. The advection velocity $\mathbf{V}_{\text{adv}}$ is the vector sum of the fluid velocity $\mathbf{V}_{\text{fluid}}$ and the so-called Nernst velocity[8] $\mathbf{V}_{\text{Nernst}}$. Advection by the Nernst effect arises because the magnetic field can move with the heat-conducting electron population and is thus proportional to the temperature gradient

$$\mathbf{V}_{\text{Nernst}} \approx -\frac{\beta_0''}{\delta_0} \frac{\tau_{ei}}{m_e} \nabla T_e, \quad (2)$$

where m_e is the electron mass, τ_{ei} is the electron-ion collision time, and β_0'' and δ_0 are Braginskii coefficients.[1] The weakly magnetized approximation (Hall parameter $\chi \ll 1$) has been implemented and for the plastic (CH) plasmas discussed herein $\beta_0''/\delta_0 \approx 2.5$. The Nernst effect contributes to the total convection of the magnetic field along with field diffusion described by the third term in Eq. (1). The first term in Eq. (1), the so-called Biermann battery or thermoelectric[9] source, is the dominant mechanism by which magnetic fields are generated in plasmas.

Much work has been done in diagnosing spontaneous electromagnetic fields in myriad laser-produced-plasma configurations: irradiated wires,[11] directly driven glass and plastic capsules,[10,12–14] inside of hohlraums,[15] and plasma bubble evolution.[16,17] The work described here extends previous observations[10] of filamentary field structures found in the corona of laser-irradiated spherical targets as discussed in Sec. II. The complexities inherent to the 3-D geometry previously investigated are alleviated through simpler face-on imaging of laser-irradiated plastic foils. The experimental methodology using both monoenergetic-protons and x-rays is discussed in Sec. III. Radiographic results of coherent 3-D cellular structure in proton images are analyzed and presented in Sec. IV. This is followed by a discussion of multiple field-generation mechanisms in Sec. V and it is

[a)]Paper QI3 3, Bull. Am. Phys. Soc. 57, 289 (2012).
[b)]Invited speaker.
[c)]Present address: Atmospheric Oceanic and Space Sciences, University of Michigan, 2455 Hayward Street, Ann Arbor, Michigan 48109, USA.
[d)]Present address: State University of New York, Geneseo, New York 14454, USA.
[e)]Also at the Department of Mechanical Engineering and Physics, 235 Hopeman Building, RC 270132, Rochester, NY 14627, USA.

demonstrated that the likely source of these fields is the magnetothermal instability (MTI) which occurs in the underdense corona. Plasma conditions in the corona are shown in Sec. VI and details of the MTI in these plasmas are discussed in Sec. VII. This article concludes with a summary of the results presented here and discusses the future directions of this work in Sec. VIII.

II. FILAMENTARY FIELDS IN THE CORONA

Monoenergetic-proton radiography[18,19] has been used to image coronal field structures in laser-irradiated CH spheres.[10] Figure 1(a) shows the experimental setup used in these experiments. A solid CH sphere with a diameter of ~860 μm was irradiated by 0.351 μm laser light with an intensity of $\sim 2 \times 10^{14}$ W/cm^2 in a 1 ns pulse that had full beam smoothing[20,21] and SG4 distributed phase plates[22] implemented on the OMEGA laser.[23] The resultant plasma blow-off was probed using 15 MeV fusion-protons provided by the backlighter capsule, discussed further in Sec. III, and images were recorded on CR-39 nuclear track detectors.[19,24]

Figure 1(b) shows four proton-fluence radiographs taken before, during, and after the 1 ns laser pulse. The field of view of the detector is 3 mm × 3 mm in each image. Protons are stopped in the solid sphere which results in the white "shadow" prevalent in each radiograph. No field structures were observed until the end (~1 ns) of the laser drive in these images. Séguin *et al*. demonstrated that the observed filamentary structures are quickly (~200 ps) generated between ~0.6 ns and ~0.8 ns in these experiments and the amplitude of proton fluence modulations was approximately constant once fields appeared. The filaments expand radially outwards with the blow-off plasma and were still visible after the drive ended.

The magnetic field evolution described by Eq. (1) indicates that fields will be advected in the direction of $\mathbf{V}_{adv}$. The advection velocity depends on both the fluid and Nernst velocities and changes as a function of position. Plasma evolution in these experiments was modeled using the 1-D radiation-hydrodynamic code LILAC[25] and the resultant velocity profiles at 1 ns are shown in Figure 1(c) as a function of distance from the ablation surface. The Nernst velocity was calculated using predicted temperature profiles in Eq. (2) and changes direction at the peak temperature as indicated in the plot. Consequently, the advection velocity changes direction in this plasma ~100 μm from the ablation front. B fields generated inside this transition region advect towards the ablation surface, otherwise they expand out with the plasma.

Filamentary structures are observed throughout the corona, thus fields must be generated in a region where they will advect out with the expanding plasma. In these images, the filaments appear to extend to the ablation surface of the sphere; however, the inherent 3-D nature of the spherical geometry precludes any definitive assessment. These images clearly demonstrate that filaments expand with the coronal plasma and are present after the laser drive has ended. The field diffusion time, $\tau_{diff} \approx (k^2 D_m)^{-1}$ where k is the wave number, may be estimated for ~100 μm size fields and is $\gtrsim$5 ns at the end of the laser drive. Thus, it is not surprising that fields are still visible ~500 ps after the drive ends. Quantitative analysis of the filament size is difficult in this geometry but was predicted[10] to be of order ~150 μm at the quarter-critical surface using Monte Carlo simulations; no difference in size was discernible at different sample times from these data. Face-on imaging of laser-irradiated planar foils has been performed to further probe these filamentary

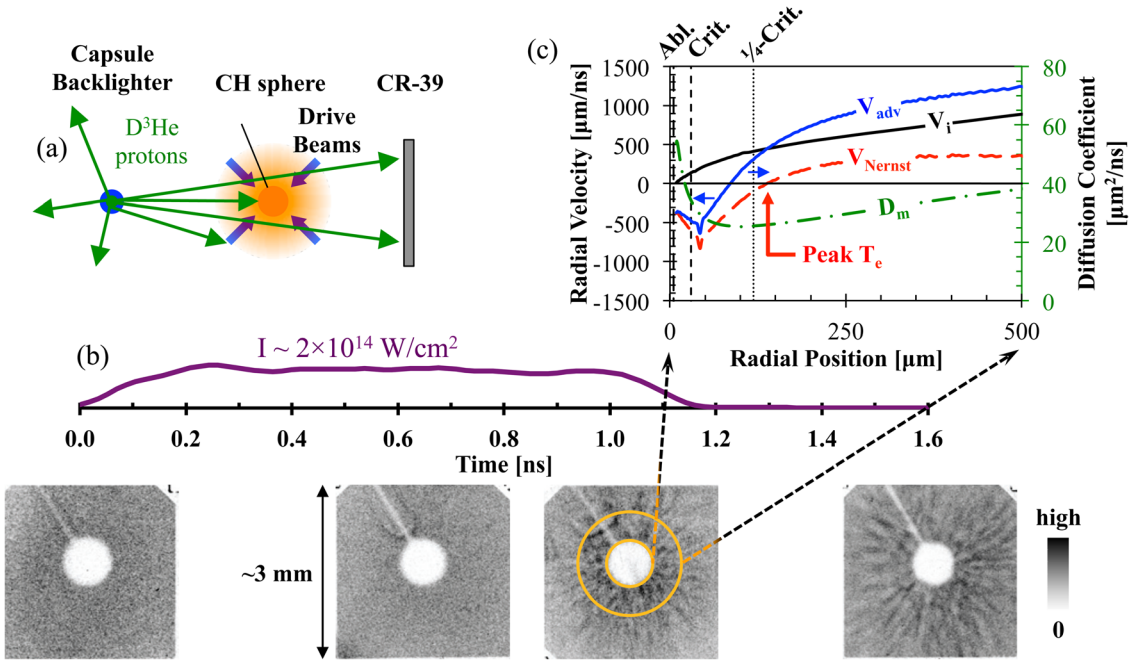

FIG. 1. (a) Experimental setup used to radiograph plasma evolution of solid CH spheres irradiated with an intensity of $\sim 2 \times 10^{14}$ W/cm^2. (b) Summary of resultant proton radiographs[10] taken during the 1 ns pulse. Darker pixels indicate higher proton fluence, but the gray scale is different in each image. (c) Profiles of the fluid, Nernst, and advection velocities calculated from 1-D radiation-hydrodynamic simulations at 1 ns. Radial distances are given relative to the ablation front and positive velocities are pointed radially outward.

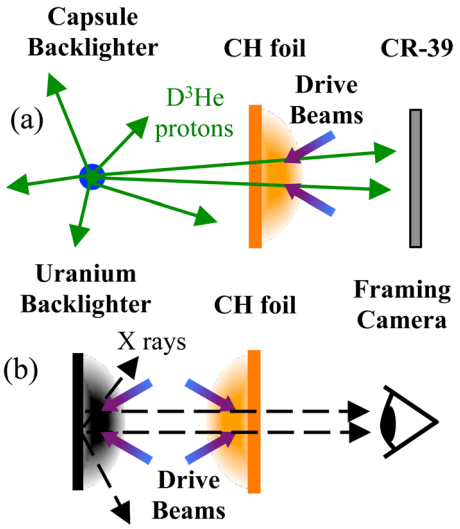

FIG. 2. A schematic drawing of the experimental setup used to radiograph directly driven plastic foils using (a) protons and (b) x rays. Proton and x-ray images were recorded on CR-39 and film, respectively.

fields on-axis and more accurately quantify their size as described below.

III. PLANAR RADIOGRAPHY EXPERIMENTS

Monoenergetic-proton and x-ray radiography experiments were performed on the OMEGA laser[23] using the configuration shown in Figure 2. Protons are sensitive to both mass and field modulations through Coulomb scattering and the Lorentz force, respectively. X rays are sensitive only to areal density modulations in the target. The complementarity of these two diagnostic techniques provides information to address density and field distributions during plasma evolution. Unlike the solid sphere experiments, planar foils will be accelerated and Rayleigh-Taylor (RT) growth of density perturbations is expected to occur. Density distributions and growth of perturbations are characterized by x-ray radiographs, whereas protons sample the path-integrated field structures.

The proton backlighter capsules, filled with 18 atm D^3He gas, were imploded using 20 OMEGA beams to produce fusion protons. Each proton radiography experiment[18,19] gives a single "snapshot" in time of the laser-foil interaction and multiple experiments with different laser timings provide a series of radiographs illustrating the plasma evolution. This backlighting technique provides a temporal resolution of $\sim$150 ps and D^3He-fusion protons ($E_p \sim 15$ MeV) are produced by an approximately Gaussian source with a FWHM of $\sim 45\ \mu$m. 15-MeV proton radiographs were recorded on filtered CR-39 plastic nuclear track detectors. After exposure, CR-39 samples were etched to reveal tracks left by the incident protons. Through the etching process, signal tracks in the plastic were revealed and pieces were scanned using an optical microscope system.[26] From these scans, radiographs were processed and proton fluence images were created.

X-ray radiographs were taken using a laser-irradiated Uranium foil to generate $\sim$1.3 keV x rays for optimum contrast through $\sim 20\ \mu$m CH. Images were recorded on film using a framing camera[27,28] with a temporal resolution of $\sim$80 ps and a spatial resolution of $\sim 10\ \mu$m. The apertured framing camera provided multiple images of a single foil during its evolution, yielding multiple radiographs from a single experiment. The measured optical depth image may be directly converted to an areal density map[27] of the target for comparison with proton radiographs that are sensitive to both density modulations and field deflections at the foil.

TABLE I. Metrology of the four CH foil types used in these experiments. Initial ambient foil density was $\rho = 1.03\ \mathrm{g/cm^3}$. Variations in thickness (l_0), wavelength (λ_0), and sinusoidal amplitude (a_0) are all $\lesssim$10 %. The value given for the eggcrate foil (3-D) is the diagonal peak-to-peak wavelength.

Label	l_0 (μm)	λ_0 (μm)	a_0 (μm)
Flat foil	21	0	0
120 μm (2-D)	21	120	0.27
180 μm (2-D)	23	180	0.55
115 μm (3-D)	26	115	0.56

Four types of CH foils of varying thicknesses and surface perturbations were used in these experiments and are listed in Table I. Foil surfaces were either flat, seeded with ridge-like 2-D sinusoidal modulations, or 3-D eggcrate-like sinusoidal modulations. The laser spot was shaped by SG4 distributed phase plates (DPPs),[22] smoothed by spectral dispersion (SSD),[20] and distributed polarization rotators (DPRs)[21] were implemented to minimize the broadband imprint from the laser spot. Twelve beams were overlapped to provide a drive intensity of $I \lesssim 4 \times 10^{14}\ \mathrm{W/cm^2}$ within a $\sim 750\ \mu$m diameter spot using a 2 ns square pulse to deliver a total of $\sim$3300 J of energy on target. Proton and x-ray radiographs were taken at times up to 2.4 ns to provide data during and after the onset of the laser drive.

IV. EXPERIMENTAL RESULTS

A. Proton radiographs

A comprehensive summary of proton-fluence radiographs is shown in Figure 3. Radiographs were taken of the four different foil types after the first nanosecond of the 2 ns laser drive. Proton fluence images of all foil types for times $\lesssim$1.5 ns indicate minor variance across the analysis region, though coherent linear features were observed in 2-D modulated foils. Previous work[29,30] has shown that these linear features are generated by Rayleigh-Taylor-induced magnetic fields caused by the growth of the preimposed surface perturbations. A rapid transition ($\lesssim$200 ps) occurs near $t \sim 1.5$ ns, whereby the fluence radiographs of all foil types show a drastic change in appearance. Some underlying linear features most likely due to RT-induced fields are still observable, especially 180-μm-foil images at times $\gtrsim$1.6 ns; however, the 3-D cellular structure is prevalent and dominates proton radiographs. These features are consistent with an axial view of the previously observed filamentary fields.

Cellular structure was shown to begin during the laser drive and continued well after the end of the pulse. The dominant scale size of these features (λ_{AC}) and the rms amplitude

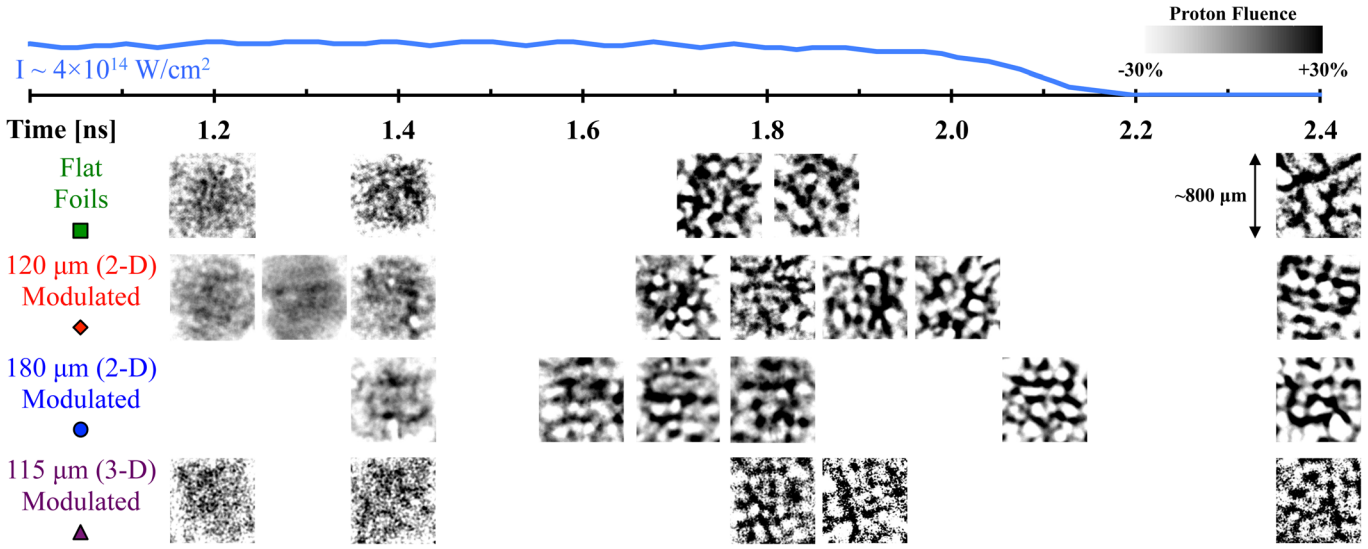

FIG. 3. Summary of proton-fluence radiographs taken of irradiated plastic foils with different initial surface perturbations. Radiographs were taken during the last nanosecond of the laser drive and after the end of the pulse. Images have been individually normalized so that the grayscale ranges from ±30% of the mean fluence in each radiograph. Cellular structures are observed in radiographs for times ≳1.6 ns irrespective of initial foil perturbations.

modulation of proton fluence (σ_{rms}) were calculated (as described in the Appendix) to characterize the scale and strength of the filamentary field structures, respectively. The results of the autocorrelation analysis are plotted in Figure 4(a). It is clearly demonstrated that these features have an approximately constant scale size that can be characterized by $\lambda_{AC} \approx 210\,\mu$m with a standard deviation of $\pm 30\,\mu$m. Radiographs taken before cellular-onset were analyzed, but did not reveal a dominant scale size and are thus not plotted in Figure 4(a). The scale of filamentary fields is shown to be constant in size immediately after initial onset and it does not measurably change in time or depend on the initial foil surface conditions. This suggests that filamentary fields are generated away from regions affected by the shape of the ablation surface, i.e., in the expanding, underdense corona.

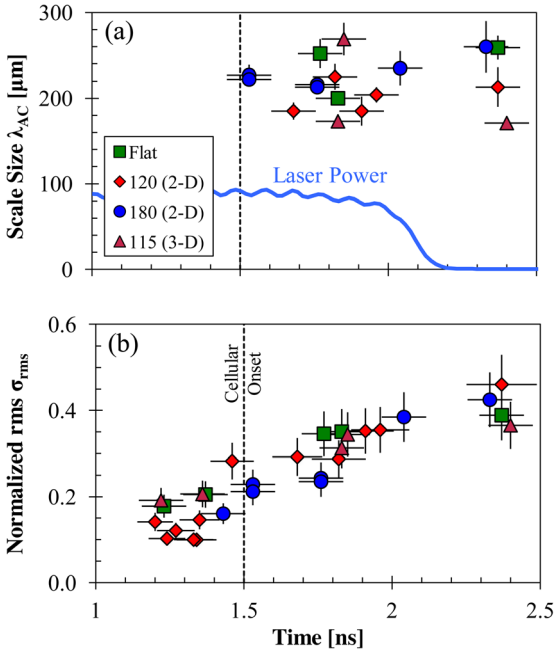

FIG. 4. (a) Dominant scale size of cellular features observed in proton radiographs as a function of time. For times ≲1.5 ns, no characteristic size was measured. (b) Normalized broadband rms amplitude of proton fluence as a function of time. The rms amplitude is shown to grow in time similarly for all foil types and continue after the laser drive has ended.

Figure 4(b) illustrates the normalized rms amplitude as a function of time for all four foil types. Radiographs at earlier times (≲1.5 ns) are shown to have normalized rms amplitudes of ≲20%, though no dominant scale size was observed. The normalized broadband rms characterizes the amplitude of proton deflections and thus path-integrated field strength. It is clearly shown that proton deflections grow at the same rate for all foil types during the laser drive. The filamentary fields causing the cellular features are created during the laser pulse, but do not lose appreciable strength ≲500 ps after the drive ends.

B. X-ray radiographs

All four foil types were radiographed with x rays to characterize density distributions in these laser-foil interactions. Modulations in areal density arise due to Rayleigh-Taylor growth of surface perturbations[28] and laser imprint.[31] X-ray radiographs shown in Figure 5(a) illustrate the evolution of areal density modulations for all target types. In these images, lighter pixels indicate higher areal density in the target (more x-ray absorption). Flat-foil radiographs show no significant features until late in time ($t \sim 2.2$ ns), at which point small-scale ($\sim 30\,\mu$m) structure due to laser imprint[32] becomes apparent. However, x-ray radiographs of modulated foils clearly show dramatic features at the seeded wavelengths due to RT growth. The perturbation amplitude of the $\lambda = 120$-μm-foil increases in time with a rate of $\gamma_{120} \sim 2\,\text{ns}^{-1}$ during the drive and these data agree well with DRACO[33] radiation-hydrodynamic simulations as shown in Figure 5(b). Some small-scale structure, also at $\sim 30\,\mu$m, is visible at late times in modulated foils, but these features are much lower in amplitude than the dominant seeded perturbations.

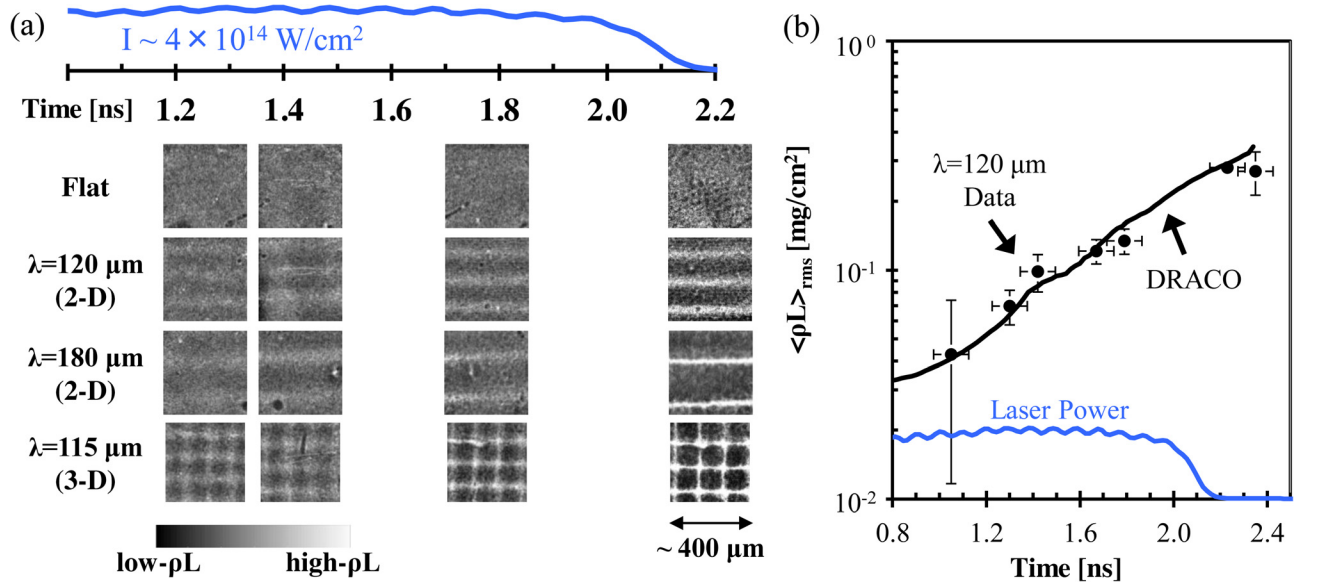

FIG. 5. (a) Summary of sample x-ray radiographs of the four different foil types. Images were taken during and after the laser drive as indicated by the image location relative to the pulse schematic. Those foils with preimposed surface modulations demonstrate RT-growth of the seeded perturbations. (b) Analysis of the 120 μm data show good agreement with radiation-hydrodynamic predictions of RT-growth.

X-ray radiographs taken at times $\gtrsim$1.5 ns do not show similar features as those observed in late-time proton fluence images. Cellular structure in areal density has been observed[31] under different experimental conditions due to laser imprint, but in experiments discussed here the 3-D structure did not have enough time to strongly develop. A Fourier analysis was performed on the x-ray images of flat and 120-μm-modulated foils at ~2.2 ns to compare the relative amplitudes of the observed features. The resultant spectra are shown in Figure 6 and demonstrate that the ~30 μm features in both cases are approximately equal in amplitude and are consistent with RT growth of laser-imprinted perturbations. In the modulated foil case, the amplitude of 120 μm perturbations is ~5 times higher than ~30 μm features.

Proton deflections due to RT-induced[29] B fields are dominated by fields at the seeded wavelength of 120 μm in the modulated foil case at times $\lesssim$1.5 ns. B fields created by RT growth occur near the ablation surface and, neglecting diffusion, are proportional to the fluid vorticity. The peak field

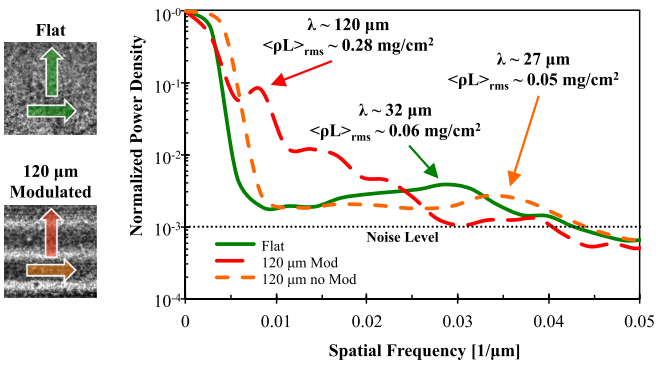

FIG. 6. X-ray images taken at ~2.2 ns of both flat and modulated foils are shown on the left. Lineout directions are indicated by arrows in the images, where spectra from multiple lineouts were averaged for the flat foil case and lineouts parallel (Mod) and perpendicular (no Mod) to the perturbation wave vector are shown for the 120 μm case.

scales[34] with perturbation parameters as $|B(t)| \propto \frac{h(t)}{\lambda\gamma}$, where h is the perturbation amplitude, λ is the wavelength, and γ is the growth rate. Proton deflections, though, are proportional to the *path-integrated* field strength $\langle BL_B \rangle$ where the field scale length $L_B \sim h$.[30] Measured RT growth rates[28] for both wavelengths, $\gamma_{30} \sim 4.5\,\text{ns}^{-1}$ and $\gamma_{120} \sim 2\,\text{ns}^{-1}$, were used with the fact that $h \propto \langle \rho L \rangle_{rms}$ to estimate the relative magnitudes of $\langle BL_B \rangle$ between the two perturbation wavelengths. If proton deflections late in time were due only to RT-induced B fields, simple estimates show that deflections due to $\lambda = 120\,\mu$m are ~15 times higher than those for $\lambda = 30\,\mu$m. This is a lower limit because diffusion effects, not included here, affect shorter wavelengths more than longer ones. Furthermore, this analysis is for images at ~2.2 ns, whereas proton images illustrate strong cellular features by ~1.7 ns. If RT-induced B fields were the dominant field structure in modulated-foil experiments, proton images would exhibit strong features consistent with surface perturbations. Instead, coherent cellular structures likely caused by filamentary fields in the underdense corona were observed in proton images at late times independent of initial surface conditions.

V. INSTABILITIES IN LASER-PRODUCED PLASMAS

Magnetic fields may be generated by a range of instabilities and sources as described in detail by Haines.[9] The primary sources are outlined in Figure 7(a) which shows where they occur in the sample plasma given by DRACO profiles at 1.5 ns. In addition to these instabilities, laser-plasma instabilities (LPI) can locally generate B fields through generation of hot-electron currents in the coronal plasma. Hard x-ray detectors[35] and scattered-light streak cameras[36] were fielded to observe LPI-related plasma behavior in the corona, though no hard x-ray or relevant scattered-light signals were observed. Filamentation of laser "hot-spots" was not responsible because the average intensity was too low[37] and all beams

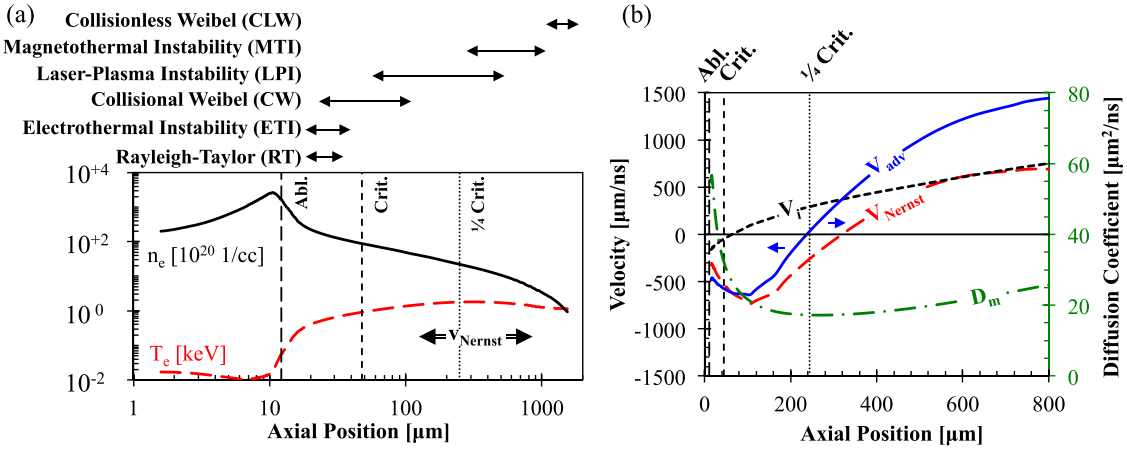

FIG. 7. (a) Predicted DRACO profiles of electron temperature and density taken at 1.5 ns. Major field-generating instabilities are listed and the locations where they occur in the plasma are indicated. The ablation, critical, and quarter-critical surfaces are labeled for reference. The absolute value of the axial position is arbitrary and a log scale is implemented to show the small-scale variation near the ablation front. The Nernst velocity changes direction at the peak temperature just outside the quarter-critical surface. (b) Profiles of the fluid, Nernst, and advection velocities calculated from DRACO simulations. Distances are given relative to the ablation front and positive velocities are pointed outward.

were spectrally smoothed.[20] LPI-generated hot-electron currents are not the source of these coherent field structures.

The so-called Weibel[38] instability is generated by electron-temperature anisotropy in the plasma. The typical collisionless form (CLW) of this instability is only relevant at the very edge of the corona[9] when $\lambda_{mfp}/(c/\omega_{pe}) \gtrsim 10^3$, where c/ω_{pe} is the collisionless skin depth. In these experiments, this parameter is $\lesssim$500 and thus CLW is a very unlikely field source. The collisional Weibel (CW) instability, which occurs in the denser plasma regions, has been predicted to generate fields under ablatively driven conditions.[39] Fields created by the CW tend to grow fastest near the over dense region ($n_e \gtrsim n_{crit}$), but when the Nernst effect and field diffusion were included, the instability was shown to be stabilized. Nonetheless, if these fields exist under the specific experimental conditions here, they would be confined to the overdense region and not advected outwards.

The electrothermal instability (ETI), first described by Haines,[40] occurs between the ablation and critical surfaces. This instability originates from a spatial perturbation to the background electron temperature that has a component perpendicular to the heat flux. The temperature perturbation leads to nonuniform ohmic heating due to the change in plasma resistivity, which positively feeds back on the perturbation. The fastest growing mode ($\lambda_{ETI} \sim 60\,\mu$m) is much smaller than the observed $\sim$210 μm scale size, therefore this instability is unlikely to be the source of the observed cellular fields. Furthermore, fields generated by the electrothermal instability are also confined to the high density region.

The Nernst effect in these experiments was calculated to be strongest just outside the critical surface. In the sample plasma shown in Figure 7(b) $\mathbf{V}_{\mathrm{Nernst}} \sim 700\,\mu$m/ns and is much larger[46] than the fluid velocity. Fields generated here are quickly advected towards the ablation front. This can result in amplification of the B field due to the increasing electron density, though this amplification is reduced by diffusion effects. DRACO calculations presented herein implemented the local thermal equilibrium (LTE) approximation[48] and a constant flux limiter of $f = 0.06$ which has been shown[28] to reproduce drive conditions well at intensities $\lesssim 5 \times 10^{14}$ W/cm^2. These calculations indicate that the advection velocity changes directions near the $\frac{1}{4}$-critical surface. Coherent fields observed in planar and spherical experiments must be generated where outward advection can occur.

A seed B field generated by the Biermann battery provides the source for the magnetothermal instability.[41–44] A perturbation to the background temperature profile can result in a misalignment of the temperature and density gradients, thereby creating a seed field. Anisotropic thermal conduction[1] due to the presence of this B field may act to enhance the perturbation. Classically, this instability can occur when the temperature and density gradients in the direction of heat flow are aligned; the coronal plasma outside of the peak temperature satisfies this condition. In this region the Nernst velocity is aligned with the fluid flow as shown in Figure 7 and B fields generated in this region will advect outwards. Furthermore, the fastest growing MTI modes, using the classical analysis,[41] are found to be $\lambda_{MTI} \sim 200 - 300\,\mu$m at these times, as discussed further in Sec. VII. MTI-generated B fields are consistent with the observed cellular scale size and are created in the corona where they will advect outwards. Coherent fields observed in proton radiographs are likely due to MTI in the corona.

VI. PLASMA FLOW CONDITIONS

Laser-matter interactions create plasma conditions that vary as a function of position as demonstrated in Figure 7(a). Plasma conditions go from cold ($T_e \sim 200$ eV) and dense ($n_e \sim 10^{23}$ cm^{-3}) near the ablation front to hot ($T_e \sim 2$ keV) and sparse ($n_e \sim 10^{21}$ cm^{-3}) in the corona. The fluid velocity also varies and, at the time shown in Figure 7(b), changes direction from inward flow to outward expansion just outside the critical surface. These varied conditions give rise to differences in dominant physics mechanisms.

The magnetic Reynolds number ($\mathrm{Re_m}$) relates B-field advection to diffusion in the plasma. This can be expressed

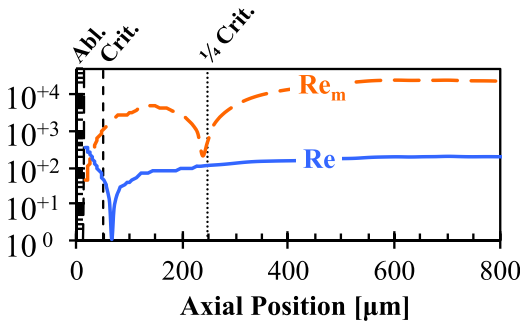

FIG. 8. Reynolds (Re) and magnetic-Reynolds (Re_m) numbers calculated from DRACO profiles at 1.5 ns. The ablation, critical, and quarter-critical surfaces are labeled for reference. The low point in Re at ~60 μm and in Re_m at ~230 μm represent where the fluid flow and advection velocity (including the Nernst effect), respectively, change directions.

as $Re_m = V_{adv}L/D_m$, where V_{adv} is the field advection velocity, L is the plasma scale length, and D_m is the field-diffusion coefficient. Figure 8 shows how Re_m varies in the plasma described in Figure 7(a) and demonstrates that in most locations, field advection dominates over diffusion. This is due to the low resistivity away from the ablation front and is consistent with B fields being frozen-in to the flow.

The Reynolds number (Re) characterizes whether the fluid flow is laminar ($Re \lesssim 2300$) or turbulent ($Re \gtrsim 4000$).[45] This dimensionless number compares inertial to viscous forces and can be written as $Re = V_{fluid}L/\nu$, where V_{fluid} is the fluid velocity, L is the plasma scale length, and ν is the kinematic viscosity of plasma ions. Figure 8 illustrates how Re changes as a function of position. The Reynolds number increases near the ablation front due to the decrease in viscosity (ν), though x-ray radiographs demonstrated coherent RT-growth at the ablation front in modulated foils during the entirety of the laser drive. These calculations demonstrate that plasma flow is dominantly laminar in nature allowing for coherent features and that B fields will be strongly advected in the underdense corona.

VII. MTI IN SPHERICAL AND PLANAR GEOMETRIES

The MTI grows from a seed magnetic field in the coronal plasma that can originate from a number of different perturbative sources, laser nonuniformities, plasma waves, etc. Thus, the initial mode distribution is not well understood or characterized and varies spatially and temporally, making quantitative analysis of this instability very difficult. Some insight may be gained, however, by examining the growth rate (γ_{MTI}) and wavelength (λ_{MTI}) of the fastest growing mode in these CH plasmas, as given by[41]

$$\gamma_{MTI} \approx 1.65 \times 10^{8} \frac{T_e^{5/2}}{n_e Z L_n L_T \ln\Lambda}\left[\frac{1}{\text{ns}}\right], \tag{3}$$

$$\lambda_{MTI} \approx 2 \times 10^{-4} \sqrt{\frac{L_n L_T Z \ln\Lambda}{n_e \lambda_D^3 T_e^{1/2}}}\ [\mu\text{m}]. \tag{4}$$

In the preceding equations, Z is the average charge state, $\ln\Lambda$ is the Coulomb logarithm, the electron temperature T_e is in keV, electron density n_e is in 10^{20} cm^{-3}, the Debye length λ_D is in μm, and the scale lengths for temperature (L_T) and density (L_n) are also in μm. Figures 9(a) and 9(b) illustrate calculations from LILAC and DRACO profiles, respectively, of λ_{MTI} (solid) and γ_{MTI} (short dashed) at single instances near the observed field-onset time. The fastest growing wavelength is very large near the peak temperature due to the long temperature scale lengths, but levels off quickly and slowly increases farther out due to decreasing densities in both the spherical and planar cases. The growth rate peaks at ~5 ns^{-1} in the planar case and decreases thereafter, whereas γ_{MTI} levels off at ~10 ns^{-1} in the spherical case before diverging at larger radii due to the rapidly decreasing density. These profiles change as a function of time, but the snap-shots shown here provide the general differences between the planar and spherical cases.

The observed onset time of the coherent field structures in planar experiments was ~2 times later than the apparent

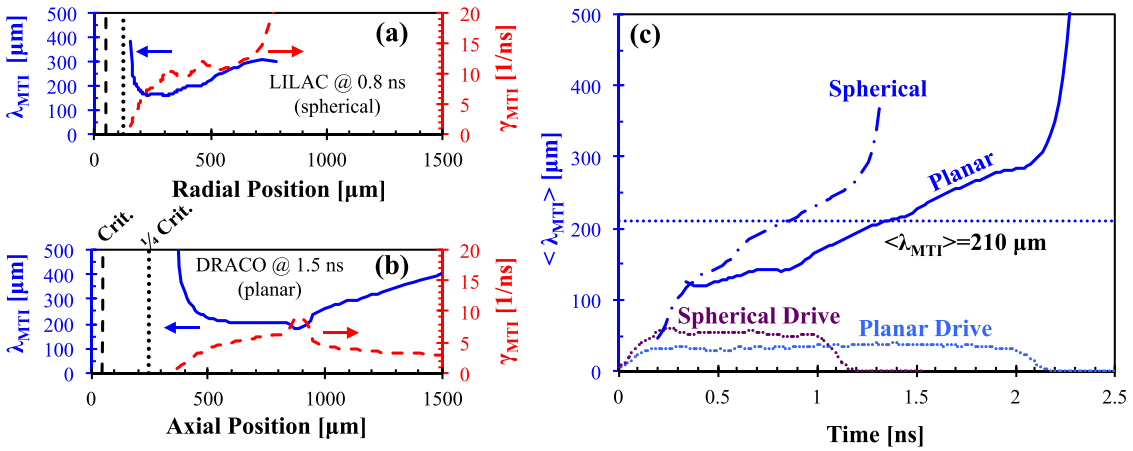

FIG. 9. The fastest growing mode growth rate γ_{MTI} (short dashed) and wavelength λ_{MTI} (solid) profiles are shown near field onset times for (a) the spherical case at 0.8 ns and (b) the planar case at 1.5 ns. Simulated profiles were used with Equations (3) and (4) to generate the curves shown here and plotted as a function of (a) radial distance and (b) axial distance. An average wavelength $\langle\lambda_{MTI}\rangle$ was calculated at each time by averaging λ_{MTI} over this space and using the growth rate as a weighting factor. (c) The resulting average wavelength as a function of time for the planar (solid) and spherical (dashed-dotted) cases with the respective drives (dotted) shown at the bottom in arbitrary units. The inferred characteristic size of cellular structures determined from planar proton radiographs is also shown at $\langle\lambda_{MTI}\rangle = 210\ \mu$m.

onset in spherical experiments. The exact cause of the apparently rapid onset of these fields is not well understood. Though near the field-onset time, calculations from classic MTI theory, as shown in Figures 9(a) and 9(b), predict a growth rate ~2 times faster in spherical experiments than planar experiments, consistent with the two separate data sets. A given plasma profile provides a spectrum of "fastest growing modes" throughout the plasma, though in both the spherical and planar cases these modes are predicted to be between ~200 and 300 μm, again consistent with observations. To assess some aspect of temporal variance, an average wavelength $\langle \lambda_{MTI} \rangle$ is defined by

$$\langle \lambda_{MTI} \rangle = \frac{\sum_i \lambda_{MTI,i} \times \gamma_{MTI,i}}{\sum_i \gamma_{MTI,i}}, \tag{5}$$

where each λ_{MTI} is weighted by the associated growth rate and is summed over the MTI-unstable region in the underdense corona at each time step. The results of this calculation for both spherical and planar simulations are shown in Figure 9(c). The laser drives for both configurations are also shown (dotted) for reference and it is clear that $\langle \lambda_{MTI} \rangle$ rapidly increases after the drive turns off due to flattening of the temperature profiles as the plasma cools. These calculations suggest that MTI occurs earlier in the drive at smaller wavelengths, though this was not observed in experiments. Rather, a rapid transition (~200 ps) was demonstrated in both the spherical and planar experiments. Interestingly though, the measured characteristic size of cellular structures, ~210 μm, crosses the spherical and planar curves in Figure 9(c) near the observed onset times for each case. It is also important to note that these calculations predict a slowly varying dominant scale size in time, which was not observed. Even though no temporal growth was measured from proton radiographs, the range of values measured from separate planar experiments is consistent with the predicted ~200–300 μm during these times.

VIII. CONCLUSION

In summary, proton and x-ray radiography experiments have been performed to further investigate filamentary fields previously observed in laser-irradiated spherical targets. Planar experiments provided an axial view of the filamentary fields and show coherent cellular field structures independent of initial surface conditions, which suggests field generation in the corona. Furthermore, these filamentary fields were observed far from the ablation surface so must be generated in a region where they can be advected outwards. These coherent field structures dominate proton radiographs of planar foils at late times over other sources of electromagnetic fields.

It has been demonstrated that the likely cause for these fields is the magnetothermal instability which is predicted to produce field structures at the observed scale size. Moreover, this instability generates fields near the peak coronal temperature where they are convected outwards with the plasma. Using classical MTI theory from Tidman and Shanny, the difference in observed onset time between the two geometries may be explained through a difference in growth rate. MTI-generated fields occur due to altered heat conduction in the corona and could therefore affect heating uniformity and efficiency in directly driven targets. These results have identified the likely source of coronal fields previously observed in directly driven spherical targets. Initial calculations indicate consistency with experiments and thus motivate further numerical and experimental exploration into field-generation by this instability.

ACKNOWLEDGMENTS

The authors thank Wolf Seka and Christian Stoeckl for their help in interpreting results from the scattered-light and hard x-ray diagnostics, respectively. The authors also express their gratitude to the engineering staff at LLE for their support. The work described here was done as part of the first author's Ph.D. thesis and supported in part by NLUF (DE-NA0000877), FSC/UR (415023-G), DoE (DE-FG52-09NA29553), LLE (414090-G), and LLNL (B580243).

APPENDIX: PROTON-RADIOGRAPH ANALYSIS TECHNIQUES

The two observables of interest in proton radiographs are the characteristic spatial wavelength of the features (λ_{AC}), if one exists, and the normalized broadband rms amplitude (σ_{rms}) which is a measure of the strength of the features. The latter may be calculated from the distribution of fluence values after removing the statistical component,

$$\sigma_{\mathrm{rms}} = \frac{\sqrt{\sigma_{meas}^2 - \sigma_{stat}^2}}{\mu_{meas}}, \tag{A1}$$

where σ_{meas} is the measured statistical deviation of protons per pixel, μ_{meas} is the statistical mean proton fluence per pixel used to normalize the variation across different experiments, and σ_{stat} is the numeric statistical variation per pixel $\sim\sqrt{\mu_{meas}}$. Deducing the characteristic spatial length of the cellular features requires a more complex analysis.

An autocorrelation (AC) algorithm is used on each proton-fluence image to determine the isotropic scale-size of the observed features. This procedure begins by calculating the 2-D FFT[47] of a square region that results in a 2-D array $C(k_x,k_y)$ of complex Fourier coefficients,

$$C(k_x, k_y) = \mathcal{F}\{I(x,y)\}, \tag{A2}$$

where $\mathcal{F}$ denotes the FFT algorithm and $I(x, y)$ is the array of pixel values in the area of interest. The autocorrelation coefficients $A(x,y)$ may then be calculated directly from the Fourier coefficients,

$$A(x,y) = \mathcal{F}^{-1}\{C^* C\}, \tag{A3}$$

where C^* is the complex conjugate of the Fourier coefficient array and $\mathcal{F}^{-1}$ is the inverse FFT algorithm. The autocorrelation coefficients, as defined above, represent how well the image correlates with itself. The AC coefficients are

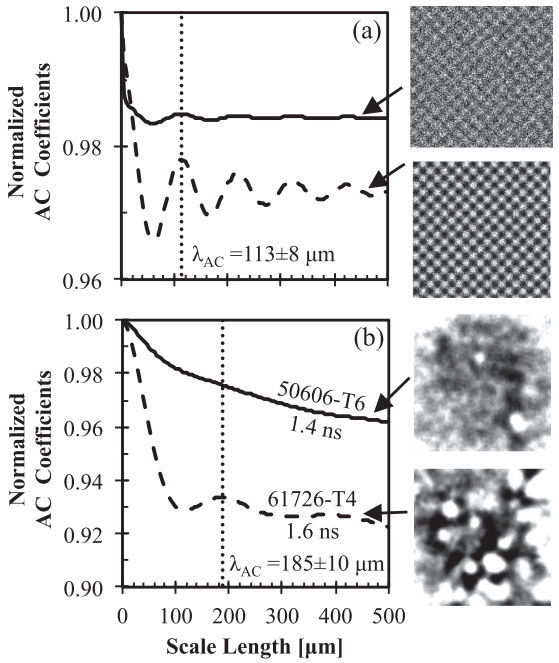

FIG. 10. (a) Two synthetic images with eggcrate-like perturbations with diagonal peak-to-peak wavelength of 106 μm and sinusoidal amplitudes of 10% (top) and 30% (bottom) of the mean. The corresponding AC spectra are shown for both images with the measured dominant scale size of the features as 113 ± 8 μm. (b) Experimental radiographs from 1.4 ns (top) and 1.6 ns (bottom) with corresponding AC spectra. The earlier image does not show a peak in the AC spectra which suggests that there is no isotropic scale size in the image. Whereas, the radiograph at 1.6 ns clearly shows a peak at 185 ± 10 μm indicating a dominant feature in the image.

azimuthally averaged in space, thus eliminating one of the spatial dimensions and producing a 1-D (radial) representation. If present, an isotropic scale-size will be revealed by this 1-D representation and may be extracted from each proton radiograph.

Figure 10 illustrates two examples of the AC analysis with synthetic data and two examples from experimental radiographs. Two synthetic images were generated with 2-D sinusoidal functions (eggcrates) of different amplitudes with a wavelength (λ_0) of 150 μm in both directions, resulting in a diagonal peak-to-peak wavelength $\lambda_{0,D} = (\sqrt{2}/2)\lambda_0$ of 106 μm. White noise with an amplitude of $\pm 20\%$ of the mean was also added. The two images in Figure 10(a) illustrate the differences between amplitudes of 10% (top) and 30% (bottom) of the mean. The corresponding normalized 1-D AC spectra are shown by the solid and dashed lines and show that higher amplitudes in the image result in higher AC coefficient values. The synthetic images used have a single spatial frequency over many wavelengths, which results in the decaying oscillations observed at harmonics of the fundamental wavelength (first peak) in the AC spectra. The dominant scale size was measured to be 113 ± 8 μm in both cases as illustrated by the dotted line. This measurement is consistent with the original diagonal peak-to-peak wavelength; AC coefficients near the lateral wavelength of 150 μm average out during this analysis. The procedure described here accurately measures the dominant scale size in these images to within the uncertainty of the measurement and with signal-to-background $\gtrsim 0.5$.

The dominant scale size of isotropic features in an image was calculated from the 1-D AC spectrum by fitting a curve to the first observed peak at a length greater than zero. A 2nd-degree polynomial was found to fit most data better than a Gaussian, or other peaked functions. The primary goal of the fit is to obtain an accurate measurement of the peak algorithmically. Furthermore, using the fitted curve, an uncertainty in the measured peak position may be estimated. The width of the peak represents the uncertainty in the dominant scale size of the observed features, though the typical FWHM metric is not a well-defined quantity in most cases. Therefore, the width of the parabola is taken at the point where it has reached 95% of the value at the peak. This width is the uncertainty in the measured scale size of cellular features.

Figure 10(b) illustrates two sample proton radiographs of laser-irradiated CH foils with ~ 120 μm ridge-like perturbations. The first image at $t \sim 1.4$ ns shows the expected linear behavior in the image and the corresponding AC coefficient spectrum (solid) does not indicate any peak after the initial fall off, suggesting that there is no dominant, isotropic scale-size. The bottom image in Figure 10(b) occurs later in time, at $t \sim 1.6$ ns, and the corresponding AC coefficient spectrum (dashed) is shown. This spectrum shows a faster fall off, indicating higher amplitude modulations than the previous image, and a dominant scale size peak at 185 ± 10 μm. This systematic analysis technique provides an accurate measurement of the dominant scale size, when present, of isotropic features observed in radiographic images.

[1]S. I. Braginskii, "Transport processes in a plasma," in *Reviews of Plasma Physics* (Consultants Bureau, New York, 1965), vol. 1.
[2]C. C. Joggerst, A. Almgren, and S. E. Woosley, "Three-dimensional simulations of Rayleigh-Taylor mixing in core-collapse supernovae," ApJ **723**, 1 (2010).
[3]H. Isobe, T. Miyagoshi, K. Shibata, and T. Yokoyama, "Filamentary structure on the Sun from the magnetic Rayleigh-Taylor instability," Nature **434**(7032), 478 (2005).
[4]G. Gregori, A. Ravasio, C. D. Murphy, K. Schaar, A. Baird, A. R. Bell, A. Benuzzi-Mounaix, R. Bingham, C. Constantin, R. P. Drake, M. Edwards, E. T. Everson, C. D. Gregory, Y. Kuramitsu, W. Lau, J. Mithen, C. Niemann, H. S. Park, B. A. Remington, B. Reville, A. P. L. Robinson, D. D. Ryutov, Y. Sakawa, S. Yang, N. C. Woolsey, M. Koenig, and F. Miniati, "Generation of scaled protogalactic seed magnetic fields in laser-produced shock waves," Nature **481**(7382), 480 (2012).
[5]J. Nuckolls, L. Wood, A. Thiessen, and G. Zimmerman, "Laser compression of matter to super-high densities: Thermonuclear (CTR) applications," Nature **239**, 139 (1972).
[6]J. A. Stamper, K. Papadopoulos, R. N. Sudan, S. O. Dean, E. A. McLean, and J. M. Dawson, "Spontaneous magnetic fields in laser-produced plasmas," Phys. Rev. Lett. **26**(17), 1012 (1971).
[7]A. Schluter and L. Biermann, "Interstellar magnetic fields," Z. Naturforsch. A **5**, 237 (1950).
[8]A. Nishiguchi, T. Yabe, and M. G. Haines, "Nernst effect in laser-produced plasmas," Phys. Fluids **28**(12), 3683 (1985).
[9]M. G. Haines, "Magnetic-field generation in laser fusion and hot-electron transport," Can. J. Phys. **64**(8), 912 (1986).
[10]F. H. Séguin, C. K. Li, M. J.-E. Manuel, H. G. Rinderknecht, N. Sinenian, J. A. Frenje, J. R. Rygg, D. G. Hicks, R. D. Petrasso, J. Delettrez, R. Betti, F. J. Marshall, and V. A. Smalyuk, "Time evolution of filamentation and self-generated fields in the coronae of directly driven inertial-confinement fusion capsules," Phys. Plasma **19**(1), 012701 (2012).
[11]M. Borghesi, L. Romagnani, A. Schiavi, D. H. Campbell, M. G. Haines, O. Willi, A. J. Mackinnon, M. Galimberti, L. Gizzi, R. J. Clarke, and S. Hawkes, "Measurement of highly transient electrical charging following high-intensity laser–solid interaction," Appl. Phys. Lett. **82**(10), 1529 (2003).

[12]O. Willi, P. T. Rumsby, and C. Duncan, "Megagauss magnetic fields on laser irradiated spherical targets," Opt. Commun. **37**(1), 40 (1981).
[13]J. R. Rygg, F. H. Séguin, C. K. Li, J. A. Frenje, M. J.-E. Manuel, R. D. Petrasso, R. Betti, J. A. Delettrez, O. V. Gotchev, J. P. Knauer, D. D. Meyerhofer, F. J. Marshall, C. Stoeckl, and W. Theobald, "Proton radiography of inertial fusion implosions," Science **319**(5867), 1223 (2008).
[14]A. Zylstra, C. Li, H. Rinderknecht, F. Séguin, R. Petrasso, C. Stoeckl, D. Meyerhofer, P. Nilson, T. Sangster, and S. Le Pape, "Using high-intensity laser-generated energetic protons to radiograph directly driven implosions," Rev. Sci. Instrum. **83**(1), 013511 (2012).
[15]C. K. Li, F. H. Séguin, J. A. Frenje, M. Rosenberg, R. D. Petrasso, P. A. Amendt, J. A. Koch, O. L. Landen, H. S. Park, H. F. Robey, R. P. J. Town, A. Casner, F. Philippe, R. Betti, J. P. Knauer, D. D. Meyerhofer, C. A. Back, J. D. Kilkenny, and A. Nikroo, "Charged-particle probing of X-ray-driven inertial-fusion implosions," Science **327**(5970), 1231 (2010).
[16]A. J. Mackinnon, P. K. Patel, R. P. Town, M. J. Edwards, T. Phillips, S. C. Lerner, D. W. Price, D. Hicks, M. H. Key, S. Hatchett, S. C. Wilks, M. Borghesi, L. Romagnani, S. Kar, T. Toncian, G. Pretzler, O. Willi, M. Koenig, E. Martinolli, S. Lepape, A. Benuzzi-Mounaix, P. Audebert, J. C. Gauthier, J. King, R. Snavely, R. R. Freeman, and T. Boehlly, "Proton radiography as an electromagnetic field and density perturbation diagnostic (invited)," Rev. Sci. Instrum. **75**(10), 3531 (2004).
[17]C. K. Li, F. H. Séguin, J. A. Frenje, J. R. Rygg, R. D. Petrasso, R. P. J. Town, P. A. Amendt, S. P. Hatchett, O. L. Landen, A. J. Mackinnon, P. K. Patel, M. Tabak, J. P. Knauer, T. C. Sangster, and V. A. Smalyuk, "Observation of the decay dynamics and instabilities of megagauss field structures in laser-produced plasmas," Phys. Rev. Lett. **99**(1), 015001 (2007).
[18]C. K. Li, F. H. Séguin, J. A. Frenje, J. R. Rygg, R. D. Petrasso, R. P. J. Town, P. A. Amendt, S. P. Hatchett, O. L. Landen, A. J. Mackinnon, P. K. Patel, V. A. Smalyuk, T. C. Sangster, and J. P. Knauer, "Measuring E and B fields in laser-produced plasmas with monoenergetic proton radiography," Phys. Rev. Lett. **97**(13), 135003 (2006).
[19]M. J.-E. Manuel, A. B. Zylstra, H. G. Rinderknecht, D. T. Casey, M. J. Rosenberg, N. Sinenian, C. K. Li, J. A. Frenje, F. H. Sguin, and R. D. Petrasso, "Source characterization and modeling development for monoenergetic-proton radiography experiments at OMEGA," Rev. Sci. Instrum. **83**(6), 063506 (2012).
[20]S. P. Regan, J. A. Marozas, J. H. Kelly, T. R. Boehly, W. R. Donaldson, P. A. Jaanimagi, R. L. Keck, T. J. Kessler, D. D. Meyerhofer, W. Seka, S. Skupsky, and V. A. Smalyuk, "Experimental investigation of smoothing by spectral dispersion," J. Opt. Soc. Am B **17**(9), 1483 (2000).
[21]T. R. Boehly, V. A. Smalyuk, D. D. Meyerhofer, J. P. Knauer, D. K. Bradley, R. S. Craxton, M. J. Guardalben, S. Skupsky, and T. J. Kessler, "Reduction of laser imprinting using polarization smoothing on a solid-state fusion laser," J. Appl. Phys. **85**(7), 3444 (1999).
[22]Y. Lin, T. J. Kessler, and G. N. Lawrence, "Distributed phase plates for super-Gaussian focal-plane irradiance profiles," Opt. Lett. **20**(7), 764 (1995).
[23]T. R. Boehly, D. L. Brown, R. S. Craxton, R. L. Keck, J. P. Knauer, J. H. Kelly, T. J. Kessler, S. A. Kumpan, S. J. Loucks, S. A. Letzring, F. J. Marshall, R. L. McCrory, S. F. B. Morse, W. Seka, J. M. Soures, and C. P. Verdon, "Initial performance results of the OMEGA laser system," Opt. Commun. **133**(1–6), 495 (1997).
[24]N. Sinenian, M. Rosenberg, M. J. E. Manuel, S. C. McDuffee, F. H. Séguin, J. A. Frenje, C. K. Li, and R. D. Petrasso, "The response of CR-39 nuclear track detector to 19 MeV protons," Rev. Sci. Instrum. **82**(10), 103303 (2011).
[25]J. Delettrez, R. Epstein, M. C. Richardson, P. A. Jaanimagi, and B. L. Henke, "Effect of laser illumination nonuniformity on the analysis of time-resolved x-ray measurements in UV spherical transport experiments," Phys. Rev. A **36**(8), 3926 (1987).
[26]F. H. Séguin, J. A. Frenje, C. K. Li, D. G. Hicks, S. Kurebayashi, J. R. Rygg, B. E. Schwartz, R. D. Petrasso, S. Roberts, J. M. Soures, D. D. Meyerhofer, T. C. Sangster, J. P. Knauer, C. Sorce, V. Y. Glebov, C. Stoeckl, T. W. Phillips, R. J. Leeper, K. Fletcher, and S. Padalino, "Spectrometry of charged particles from inertial-confinement-fusion plasmas," Rev. Sci. Instrum. **74**(2), 975 (2003).
[27]V. A. Smalyuk, T. R. Boehly, D. K. Bradley, J. P. Knauer, and D. D. Meyerhofer, "Characterization of an x-ray radiographic system used for laser-driven planar target experiments," Rev. Sci. Instrum. **70**(1), 647 (1999).
[28]V. A. Smalyuk, S. X. Hu, V. N. Goncharov, D. D. Meyerhofer, T. C. Sangster, C. Stoeckl, and B. Yaakobi, "Systematic study of Rayleigh–Taylor growth in directly driven plastic targets in a laser-intensity range from $\sim 2 \times 10^{14}$ to $\sim 1.5 \times 10^{15}$ W/cm^2," Phys. Plasma **15**(8), 082703 (2008).
[29]M. J.-E. Manuel, C. K. Li, F. H. Séguin, J. A. Frenje, D. T. Casey, R. D. Petrasso, S. X. Hu, R. Betti, J. Hager, D. D. Meyerhofer, and V. Smalyuk, "First measurements of Rayleigh-Taylor-induced magnetic fields in laser-produced plasmas," Phys. Rev. Lett. **108**(25), 255006 (2012).
[30]M. J.-E. Manuel, C. K. Li, F. H. Séguin, J. A. Frenje, D. T. Casey, R. D. Petrasso, S. X. Hu, R. Betti, J. Hager, D. D. Meyerhofer, and V. Smalyuk, "Rayleigh-Taylor-induced magnetic fields in laser-irradiated plastic foils," Phys. Plasma **19**(8), 082710 (2012).
[31]V. A. Smalyuk, O. Sadot, J. A. Delettrez, D. D. Meyerhofer, S. P. Regan, and T. C. Sangster, "Fourier-space nonlinear Rayleigh-Taylor growth measurements of 3D laser-imprinted modulations in planar targets," Phys. Rev. Lett. **95**(21), 215001 (2005).
[32]S. X. Hu, G. Fiksel, V. N. Goncharov, S. Skupsky, D. D. Meyerhofer, and V. A. Smalyuk, "Mitigating laser imprint in direct-drive inertial confinement fusion implosions with high-Z dopants," Phys. Rev. Lett. **108**(19), 195003 (2012).
[33]P. B. Radha, V. N. Goncharov, T. J. B. Collins, J. A. Delettrez, Y. Elbaz, V. Y. Glebov, R. L. Keck, D. E. Keller, J. P. Knauer, J. A. Marozas, F. J. Marshall, P. W. McKenty, D. D. Meyerhofer, S. P. Regan, T. C. Sangster, D. Shvarts, S. Skupsky, Y. Srebro, R. P. J. Town, and C. Stoeckl, "Two-dimensional simulations of plastic-shell, direct-drive implosions on OMEGA," Phys. Plasma **12**(3), 032702 (2005).
[34]B. Srinivasan and X.-Z. Tang, "Mechanism for magnetic field generation and growth in Rayleigh-Taylor unstable inertial confinement fusion plasmas," Phys. Plasma **19**(8), 082703 (2012).
[35]C. Stoeckl, R. E. Bahr, B. Yaakobi, W. Seka, S. P. Regan, R. S. Craxton, J. A. Delettrez, R. W. Short, J. Myatt, A. V. Maximov, and H. Baldis, "Multibeam effects on fast-electron generation from two-plasmon-decay instability," Phys. Rev. Lett. **90**(23), 235002 (2003).
[36]W. Seka, D. H. Edgell, J. P. Knauer, J. F. Myatt, A. V. Maximov, R. W. Short, T. C. Sangster, C. Stoeckl, R. E. Bahr, R. S. Craxton, J. A. Delettrez, V. N. Goncharov, I. V. Igumenshchev, and D. Shvarts, "Time-resolved absorption in cryogenic and room-temperature direct-drive implosions," Phys. Plasma **15**(5), 056312 (2008).
[37]D. Pesme, S. Hller, J. Myatt, C. Riconda, A. Maximov, V. T. Tikhonchuk, C. Labaune, J. Fuchs, S. Depierreux, and H. A. Baldis, "Laser-plasma interaction studies in the context of megajoule lasers for inertial fusion," Plasma Phys. Controlled Fusion **44**(12B), B53 (2002).
[38]E. S. Weibel, "Spontaneously growing transverse waves in a plasma due to an anisotropic velocity distribution," Phys. Rev. Lett. **2**(3), 83 (1959).
[39]E. M. Epperlein and A. R. Bell, "Non-local analysis of the collisional Weibel instability in planar laser-ablated targets," Plasma Phys. Controlled Fusion **29**(1), 85 (1987).
[40]M. G. Haines, "Thermal instability and magnetic field generated by large heat flow in a plasma, especially under laser-fusion conditions," Phys. Rev. Lett. **47**(13), 917 (1981).
[41]D. A. Tidman and R. A. Shanny, "Field-generating thermal instability in laser-heated plasmas," Phys. Fluids **17**(6), 1207 (1974).
[42]M. Ogasawara, A. Hirao, and H. Ohkubo, "Hydrodynamic effects on field-generating thermal instability in laser-heated plasma," J. Phys. Soc. Jpn. **49**(1), 322 (1980).
[43]A. Hirao and M. Ogasawara, "Magnetic field generating thermal instability including the Nernst effect," J. Phys. Soc. Jpn. **50**, 668 (1981).
[44]J. J. Bissell, R. J. Kingham, and C. P. Ridgers, "Magnetothermal instability in laser plasmas including hydrodynamic effects," Phys. Plasmas **19**(5), 052107 (2012).
[45]J. Holman, *Heat Transfer* (McGraw-Hill, 2002).
[46]L. Willingale, A. G. R. Thomas, P. M. Nilson, M. C. Kaluza, S. Bandyopadhyay, A. E. Dangor, R. G. Evans, P. Fernandes, M. G. Haines, C. Kamperidis, R. J. Kingham, S. Minardi, M. Notley, C. P. Ridgers, W. Rozmus, M. Sherlock, M. Tatarakis, M. S. Wei, Z. Najmudin, and K. Krushelnick, "Fast advection of magnetic fields by hot electrons," Phys. Rev. Lett. **105**(9), 095001 (2010).
[47]W. H. Press, S. A. Teukolsky, W. T. Vetterling, and B. P. Flannery, *Numerical Recipes in C++: The Art of Scientific Computing*, 2nd ed. (Cambridge University Press, 2002).
[48]Recent work by Willingale *et al.*[46] demonstrated B field advection due to the Nernst effect at speeds $\sim$8000 μm/ns. Though, these experiments had I $\sim 10^{15}$ W/cm^2 with $\lambda = 1.053\,\mu$m, whereby hot-electron generation is more prominent and nonlocal thermal conduction plays a significant role.